Conductivity in lead substituted bismuth yttrate fluorites

A. Borowska-Centokowska,[1] X. Liu,[2] M. Holdynski,[3] M. Malys,[1] S. Hull,[4]
F. Krok,[1] W.Wobel,[1*] and I. Abrahams[2*]

[1]Faculty of Physics, Warsaw University of Technology, Koszykowa 75,
00-662 Warszawa, Poland.

[2]Materials Research Institute, School of Biological and Chemical Sciences, Queen Mary University of London, Mile End Road, London E1 4NS, U.K.

[3]Institute of Physical Chemistry, Polish academy of Sciences, Kasprzaka 44/52, 01-224 Warsaw, Poland.

[4]STFC ISIS Facility, Rutherford Appleton Laboratory, Chilton, Didcot, Oxon OX11 0QX, UK

*Corresponding authors: I. Abrahams e –mail: i.abrahams@qmul.ac.uk
W. Wrobel e–mail: wrobel@if.pw.edu.pl

Abstract

The di-substituted bismuth oxide based oxide ion conducting electrolyte system $Bi_{2.5+x}Pb_{0.5}YO_{5.75+3x/2-\delta}$ (x = 0, 1 and 2) has been investigated by X-ray powder diffraction, a.c. impedance spectroscopy, thermal analysis and X-ray photoelectron spectroscopy. δ-Bi_2O_3 type phases are observed for all compositions studied and showed no obvious changes in structure up to 850°C. Results from thermal analysis, and the thermal variation of the lattice parameter indicate a small degree of reduction occurs at high temperature, which is preserved on quenching. XPS results suggest this involves reduction of bismuth and lead cations. This reduction is reversed on heating at intermediate temperatures. The redox reactions appear to be correlated to a degree of curvature in the Arrhenius plot of conductivity. Measurement of transference numbers indicate that these materials are predominantly ionic conductors, with conductivity values at high temperature comparable with mono-substituted analogues.

Keywords:

Bismuth oxide; bismuth lead yttrium oxide; fluorite structure, neutron diffraction; X-ray diffraction; ac impedance spectroscopy, transference number, XPS.

1. Introduction

Oxide ion conducting solid electrolytes continue to be of interest as materials for solid oxide fuel cells (SOFCs), gas separation membranes and oxygen pumps. The highest known oxide ion conductivity is observed above 730°C for the high temperature δ-polymorph of bismuth oxide [1]. The structure of δ-Bi_2O_3 may be described as that of a defect fluorite, i.e. *ccp* Bi^{3+} cations with O^{2-} in ¾ of the tetrahedral sites. δ-Bi_2O_3 therefore has a very high vacancy concentration of 0.5 vacancies per metal atom. This feature, combined with the high polarizability of bismuth [2] and three dimensional conduction pathways, leads to the very high oxide ion conductivity of this phase. On cooling, δ-Bi_2O_3 undergoes phase transitions to more poorly conducting phases [3]. However, the highly disordered fluorite structure can be preserved to lower temperatures through solid solution formation with other metal oxides [4-9]. The size and valency of the substituting cation is known to play a key role in δ-phase stabilisation, with high conductivity and wide solid solution limits observed for materials substituted by those rare earth metals, which have an atomic radius comparable to that of Bi^{3+} [10]. Substituted bismuth oxide based fluorites often show instabilities at moderate temperatures, which depend on the ionic radius of the metal dopant and its polarizability [11-13]. These thermal instabilities, along with instability at reduced oxygen partial pressures, have limited their direct application in fuel cells. However, it has recently been shown that with suitable device construction these materials can indeed be used in SOFCs and offer suitable performance at intermediate temperatures [14].

Extensive research has been carried out on binary systems of the type Bi_2O_3-MO_x [e.g.4-13]. It has been shown that di-substitution of bismuth in ternary systems can result in: (i) stabilisation of the δ-phase to low temperatures, where similar levels of a single substituent do not; and (ii) enhanced stability of the δ-phase at intermediate temperatures [15-18]. The former has been explained in terms of an increase in configurational entropy [19]. We have previously studied a number of ternary systems of the type Bi_2O_3-RE_2O_3-Nb_2O_5 (where RE = Y, Yb, Er) [20-22]. In these systems, involving isovalent and supervalent substituents, the vacancy concentration per metal atom is less than or equal to that in δ-Bi_2O_3. Subvalent substitution of bismuth by Pb^{2+} represents an attractive option, since it offers the possibility of increasing the nominal vacancy concentration per metal atom beyond that in pure δ-Bi_2O_3. Pb^{2+} ions show many similarities to Bi^{3+}, with similar stereochemical activity of the $6s^2$ electron pairs, comparable polarizabilities (α_D = 46 and 50 a.u., respectively, for the neutral atoms of Pb and Bi [23]) and adoption of similar distorted coordination environments in oxide systems. Despite these apparent similarities the cubic δ-phase in the Bi_2O_3-PbO binary system is only observed at elevated temperatures [24]. However, in ternary systems of

the type Bi_2O_3-MO_x-PbO (M = Ca, Y, Er and La) it has been shown that δ-type phases can be preserved to room temperature [25-30].

In the present study, the thermal dependence of structure and conductivity in the di-substituted system $Bi_{2.5+x}Pb_{0.5}YO_{5.75+3x/2}$ has been investigated. In the only previous study of the Bi_2O_3-Y_2O_3-PbO system, that we are aware of, δ-type phases were quenchable over a large compositional range, with compositions exhibiting very high conductivities [27].

2. Experimental

2.1 Sample preparations

Samples of general composition $Bi_{2.5+x}Pb_{0.5}YO_{5.75+3x/2-\delta}$ (x = 0, 1 and 2) were prepared using stoichiometric amounts of Bi_2O_3 (Sigma Aldrich, 99.9%), PbO (Sigma Aldrich, 99.99%) and Y_2O_3 (Sigma Aldrich, 99.99%). The starting mixtures were ground in ethanol using a planetary ball mill and the dried mixtures were heated in air at 650°C for 20 h, then cooled and reground in an agate mortar. The samples were then heated at 800°C for 24 h and quenched to room temperature. For electrical measurements, samples were subsequently reground in the ball mill, dried and pelletised. Pellets were pressed isostatically at a pressure of 400 MPa and heated to 850°C for 15 h before quenching in air to room temperature.

2.2 Electrical measurements

Electrical parameters were determined by a.c. impedance spectroscopy up to *ca*. 840°C using a fully automated Solartron 1255/1286 system, in the frequency range 1 Hz to 5×10^5 Hz. Samples for impedance measurements were prepared as rectangular blocks (*ca.* $6 \times 3 \times 3$ mm^3) cut from quenched sintered pellets using a diamond saw. Platinum electrodes were sputtered by cathodic discharge on the two smallest faces. Impedance spectra were acquired over two cycles of heating and cooling at stabilised temperatures. Impedance at each frequency was measured repeatedly until consistency (2% tolerance in drift) was achieved or a maximum number of 25 repeats had been reached, using an algorithm described earlier [31].

The ionic and electronic contributions to the total conductivity were measured using a modified EMF method, with an external adjustable voltage source in the concentration cell O_2($pO_2 = 1.01 \times 10^5$ Pa): Pt | oxide | Pt : O_2 ($pO_2 = 0.2095 \times 10^5$ Pa) as described in detail elsewhere [32]. Measurements were performed on cooling between 800°C and 500°C at stabilized temperatures.

2.3 Diffraction

X-ray powder diffraction data were obtained on a PANalytical X'Pert Pro diffractometer fitted with an X'Celerator detector, using Ni filtered Cu-Kα radiation (λ_1 = 1.54056 Å and λ_2 = 1.54439 Å). Data were collected in flat plate θ/θ geometry and calibrated against an external LaB_6 standard. Room temperature data suitable for detailed Rietveld refinement were collected in the 2θ range 5-120°, in steps of 0.0167°, with an effective scan time of 400 s per step. Elevated temperature measurements were made using an Anton Paar HTK-1200 camera. Samples were mounted on a Pt coated ceramic sample holder and data collected in steps of 50°C from 100°C to 850°C in the 2θ range 5-120°, with a step width of 0.033°, with an effective scan time of 200 s per step for the scans at 500°C and 700°C and 50 s per step for all other temperatures. Unit cell parameters were determined by Rietveld analysis using the GSAS suite of programs [33]. A cubic model in space group *Fm*-3*m* was used for all refinements with Bi, Pb and Y located on the ideal 4*a* site (0,0,0) [20].

2.4 Thermal Analysis

Simultaneous differential thermal analysis (DTA) and thermogravimetric analysis (TGA) were carried out using a TA Instruments Q600 scanning differential thermal analyzer. Measurements were performed using *ca*. 50 mg of sample in an alumina crucible over heating and cooling runs in air, from room temperature to 850°C, at a rate of 20°C min^{-1}. Thermal events are recorded here as event maxima.

2.5 X-ray photoelectron spectroscopy

X-ray photoelectron spectroscopy (XPS) measurements were performed on pelletised samples of the studied compositions using a Thermo Scientific Microlab 350 spectrometer, with Al-Kα non-monochromated radiation (1486.6 eV; 100 W) as the excitation source. Measurements were performed on quenched samples and slow cooled, with sample pellets heated to 850°C for 10 h and quenched or slow cooled in air to room temperature, accordingly. Pellets were then polished with abrasive paper (800 grade), cleaned by sonication in an ethanol bath, and stored in a dessicator. The pressure during analysis was 5.0×10^{-9} mbar. The binding energies of the target elements (Bi 4*f*, Pb 4*f*, Y 3*d*, O 1*s*) were determined at a pass energy of 40 eV, with a resolution of 0.83 eV, using the binding energy of carbon (C 1*s*: 285.0 ± 0.2 eV) as a reference. A Shirley [34] background subtraction was applied to obtain the XPS signal intensity. Data were corrected for surface charging effects, prior to fitting using an asymmetric Gaussian/Lorentzian function.

3. Results and Discussion

X-ray powder diffraction patterns confirm that the fluorite structure is maintained throughout the studied compositional range ($0 \leq x \leq 2$) and at all temperatures investigated. Representative diffraction patterns are shown in Fig. 1. The refined unit cell parameter is seen to show a linear increase with increasing average cation radius (Fig. 2) and is consistent with solid solution formation. The thermal variation of cubic lattice parameter on heating and cooling was similar in all the studied compositions (Fig. 3). The heating and cooling profiles can be divided into three approximately linear regions. On heating, the data show a linear thermal expansion of the lattice parameter up to *ca*. 350°C; a second region extends from about 450°C to *ca*. 600°C, with a high temperature linear region above *ca*. 600°C. On cooling, the profile matches that on heating up to *ca*. 450°C, but below this temperature shows significantly smaller values for the lattice parameter than those observed on heating. The percentage change in room temperature lattice parameter between heating and cooling runs decreases with increasing *x*-value (0.20, 0.17 and 0.14 % for x = 0, 1 and 2, respectively).

The DTA thermograms for the studied compositions are shown in Fig. 4 and show no gross thermal events. However, close inspection of the thermograms in the region 200 to 700°C (inset Fig. 4), reveals two broad endothermic events on heating. Table 1 summarises the temperatures of observed thermal events, which appear to correspond to the transition temperatures between the three regions, seen in the thermal expansion of cubic lattice parameter. On cooling, all DTA thermograms were featureless. On heating, TGA reveals that samples start to gain mass at *ca*. 350°C, reaching a maximum at *ca*. 530°C and then loose mass up to *ca*. 750°C (Fig. 5). On cooling a steady mass increase is observed down to *ca*. 350 to 400°C. In all samples, the observed mass changes were very small and decreased with increasing x value (0.21, 0.14 and 0.07 % for x = 0, 1 and 2, respectively).

The observed mass changes correlate well with the changes seen in the thermal variation of lattice parameter and may be associated with redox processes in the sample. At high temperatures it is expected that a small degree of reduction occurs and quenching of samples preserves this situation to room temperature. From the observed mass changes, the value of δ, which describes the degree of oxygen non-stoichiometry per formula unit, is calculated to be in the order of 0.1 (assuming samples contain only Bi^{3+} and Pb^{2+} after thermal cycling). On initial heating of the samples above *ca.* 350°C, there is sufficient thermal energy for re-oxidation to occur, accompanied by an increase in mass. Two factors control the unit cell volume during this process: (i) the average cation radius decreases with increasing level of oxidation and (ii) the unit cell accommodates an increasing oxide ion content. In combination with the effect of temperature, the latter process would be expected to result in a positive deviation in the thermal expansion of the lattice parameter, while

the former would yield a negative deviation. It is evident from the results presented in Fig. 3 that it is the decrease in average cation radius that dictates the change in lattice dimension during the oxidation process, with a small step seen between *ca*. 400 and 450°C. This can be explained by considering the high oxide ion vacancy concentration in this system, which readily accommodates additional oxide ions without significant lattice expansion.

Above *ca*. 450°C the TGA results are consistent with a small degree of reduction, which is accompanied by a positive deviation in the lattice parameter variation, reflecting the larger average cation radius. On slow cooling, in the DTA and XRD experiments, oxidation occurs, with the sample gaining mass and exhibiting a smaller unit cell parameter at room temperature than is observed on initial heating. There is a reasonable correlation between the observed percentage mass change for each composition (Fig. 5) and the relative change in room temperature lattice parameter between heating and cooling cycles (Fig. 3).

In order to shed more light on the nature of the redox processes in this system, XPS spectra were collected on the studied compositions (Fig. 6). We have previously shown that even small changes in the average oxidation state for particular cations can be reflected in weak, but measurable, shifts in the average binding energies for the corresponding atoms [36]. The measured binding energies for the cations are summarised and compared to literature values in Table 2. Binding energies of the bismuth $4f_{7/2}$ and $4f_{5/2}$ electrons are within the range quoted for pure Bi_2O_3. Similarly, those observed for lead lie close to those for PbO. The binding energies for bismuth and lead are lower in slow cooled samples compared to quenched samples of the same composition. The Y $3d_{5/2}$ peak partly overlaps with that for Bi $4f_{7/2}$ (Fig. 6a) and therefore the estimated standard deviations on the yttrium binding energies are significantly larger than those for Bi and Pb. The Y $3d_{5/2}$ binding energy is equal within two standard deviations between quenched and slow cooled samples and compare well to literature values for Y_2O_3. The O 1*s* core level photoemission spectra were fitted to three components (Fig. 6c) located at 530.1(6) eV and 531.9(8) eV and 533.3(9) eV. The lower binding energy O 1*s* peak corresponds to the regular lattice oxygen, while the higher energy peaks indicate a degree of surface carbonation.

A decrease in average binding energy would normally be considered to indicate an increase in average oxidation state. However, the binding energies for Pb $4f_{7/2}$ and $4f_{5/2}$ electrons in PbO lie above the literature values for both metallic lead and PbO_2. This apparent anomaly in the binding energies for lead oxides has previously been discussed [37]. In the case of bismuth, there are discrepancies in the literature binding energies for $NaBiO_3$. Morgan *et al*. [38] found that the values for the binding energies of Bi 4*f* electrons in $NaBiO_3$ were greater than those for Bi_2O_3, while in a more recent study, Kostikova *et al.* [39] found that the binding energy of the Bi $4f_{7/2}$ electron in $NaBiO_3$ lay in between those of metallic bismuth and Bi_2O_3, in a similar way to the situation in lead

oxides. In order to explain the observed trends in binding energy for lead and bismuth in the present system, it is helpful to consider the thermogravimetric results, which appear to confirm a degree of reduction in the quenched samples, that appears to correlate with the changes observed in lattice parameter. In the case of bismuth, this reduction could correspond to a reduction from Bi^{3+} or from a residual amount of Bi^{5+}. Reduction of Bi^{3+} to Bi^{2+} or Bi^{+} is not unknown, for example BiO has been isolated and crystallographically characterised [40], while hydrated Bi^{+} has been observed in the gas phase [41]. In studies on lead calcium bismuth oxide, Drache *et al*. [26] have argued that Bi^{5+} is the species that is reduced. Based on the results in the present study and the discrepancy in the literature values for Bi^{5+}, it is impossible to distinguish between these two cases. Similarly, it is difficult to confirm that Pb^{4+} is reduced to Pb^{2+} rather than Pb^{2+} to Pb^{+}. Pb^{+} has proven to be an elusive species. Although the crystal structure of Pb_2O was reported in 1926 [42], there are serious doubts as to the true oxygen stoichiometry in that work. However, evidence for monovalent lead has been found in lead hydride cations, using EPR spectroscopy [43] and lead hydrate cations, using mass spectrometry [44].

The Arrhenius plots of total conductivity for all studied compositions are fully reproducible between subsequent heating and cooling runs; those for the second cooling run are shown in Fig. 7. All plots are similar in shape and show a degree of curvature over a wide temperature range: *ca*. 350°C to *ca.* 700°C. This range appears to correlate with the intermediate temperature region observed in the thermal variation of lattice parameter and that in the TGA experiments, where mass change is seen to occur. While the redox processes associated with the mass change will alter the number of charge carriers in this system, it is probable that the biggest effect on conductivity is due to the change in lattice parameter caused by the redox processes, which directly affects ion mobility. The activation energies of the low temperature and high temperature linear regions, ΔE_{LT} and ΔE_{HT}, respectively and conductivities at characteristic temperatures within these two regions, 300°C (σ_{300}) and 800°C (σ_{800}), are given in Table 3. At high temperatures, all compositions exhibit high conductivity, with a maximum for the x = 1 composition. The conductivity values for $Bi_{2.5}Pb_{0.5}YO_{5.75}$ are about an order of magnitude lower than those for the lead free analogue Bi_3YO_6 at low temperature [45]. However, the high temperature conductivity values are comparable. This suggests that any increase in conductivity, as a result of the increase in vacancy concentration in the lead substituted system, is compensated for by defect trapping effects associated with the dopant cations.

Fig. 8 shows the separate contributions of ionic and electronic conductivity to total conductivity for two of the studied compositions. The results confirm that the materials are predominantly ionic conductors above *ca*. 450°C, with transference number values close to 100% for both compositions.

Conclusions

Di-substitution of lead and yttrium for bismuth in Bi_2O_3 leads to formation of δ-Bi_2O_3 type phases, with nominally higher vacancy concentrations than in pure δ-Bi_2O_3. All the compositions studied show a small degree of reduction at high temperatures, which is preserved on quenching. On reheating, re-oxidation occurs at intermediate temperatures, which is reflected in the unit cell parameter variation and the Arrhenius plot of conductivity. XPS results suggest that this predominantly involves the lead and bismuth cations. Redox reactions similar to those observed in the present system are likely to be a common feature in bismuth oxide based materials and may well be associated with the commonly observed instability of these materials at intermediate temperatures.

Although the $Bi_{2.5+x}Pb_{0.5}YO_{5.75+3x/2-\delta}$ system exhibits lower conductivity than the mono-substituted bismuth yttrate system at low temperatures, the high temperature conductivities are comparable, with transference numbers close to unity indicating predominantly ionic conductivity.

Acknowledgements

This work has been supported by the European Union in the framework of the European Social Fund through the Warsaw University of Technology Development Programme, realized by the Centre for Advanced Studies. WW and ABC wishes to thank the National Science Centre, Poland for project grant number 2012/05/E/ST3/02767 and 2011/01/N/ST5/03263. We are grateful to Dr R. M. Wilson at Queen Mary University of London for his help in X-ray data collection.

References

1. T. Takahashi, H. Iwahara, Y Nagaj, *J. Appl. Electrochem*., 2 (1972) 97.
2. D.S. Aidhy, S.B. Sinnott, E.D. Wachsman, S.R. Phillpot, *Ionics*, 16 (2010) 297.
3. H.A. Harwig, A.G. Gerards, *J. Solid State Chem*., 26 (1978) 265.
4. G. Mairesse, in Fast Ion Transport in Solids, B. Scrosati, A. Magistris, C.M. Mari, G. Mariotto (Eds.), Kluwer Academic Publishers, Dordrecht, 1993, p271.
5. J.C. Boivin, G. Mairesse, *Chem. Mater*., 10 (1998) 2870.
6. P. Shuk, H.D. Wiemhöfer, U. Guth, W. Göpel, M. Greenblatt, *Solid State Ionics*, 89 (1996) 179.
7. N.M. Sammes, G.A. Tompsett, H. Näfe, F. Aldinger, *J. Eur. Ceram. Soc*., 19 (1999) 1801.
8. A.M. Azad, S. Larose, S.A. Akbar, *J. Mater. Sci*., 29 (1994) 4135.
9. M. Drache, P. Rooussel, J-P. Wignacourt, *Chem. Rev*., 107 (2007) 80
10. H. Iwahara, T. Esaka, T. Sato, T. Takahashi, *J. Solid State Chem*., 39 (1981) 173.

11. A.A. Yaremchenko, V. V Kharton, E.N. Naumovich, A.A. Tonoyan, *Mater. Res. Bull*., 35 (2000) 515.

12. N. Jiang, E.D. Wachsman, *J. Amer. Ceram. Soc*., 64 (1999) 3057.

13. E.D. Wachsman, *J. Eur. Ceram, Soc*. 24 (2004) 1281.

14. E.D. Wachsman, K.T. Lee, *Science,* 334 (2011) 935.

15. A. Watanabe, M. Sekita, *Solid State Ionics*, 176 (2005) 2429.

16. K.Z. Fung H.D. Baek, A. Virkar, *Solid State Ionics*, 52 (1992) 199.

17. K. Huang, M. Feng, J. B. Goodenough, *Solid State Ionics*, 89 (1996) 17.

18. N. Jiang, E.D. Wachsman, S.-H. Jung, *Solid State Ionics*, 150 (2002) 347.

19. G. Meng, C. Chen, X. Han, P. Yang, D. Peng, *Solid State Ionics*, 28-30 (1988) 533.

20. I. Abrahams, A. Kozanecka-Szmigiel, F. Krok, , W. Wrobel, S.C.M. Chan, J.R. Dygas, *Solid State Ionics*, 177 (2006) 1761.

21. M. Leszczynska, X. Liu, W. Wrobel, M. Malys, M. Krynski, S. T. Norberg, S. Hull, F. Krok, I. Abrahams, *Chem. Mater*. 25 (2013) 326

22. M. Leszczynska, M. Holdynski, F. Krok, I. Abrahams, X. Liu, W. Wrobel, *Solid State Ionics,* 181 (2010) 796.

23. G. Maroulis, Computational Aspects of Electric Polarizability Calculations: Atoms, Molecules and Clusters, Imperial College Press, 2006.

24. N.M. Sammes, G. Tompsett, R. Phillips, C. Carson, A.M. Cartner, M.G. Fee, *Solid State Ionics*, 86-88 (1996) 125.

25. M. Drache, P. Conflant, J.C. Boivin, *Solid State Ionics*, 57 (1992) 245.

26. M. Drache, J.C. Schrotter, P Conflant, *J. Mater. Chem*., 3 (1993) 789.

27. M. Omari, M. Drache, P. Conflant, J.C. Boivin, *Solid State Ionics*, 40/41 (1990) 929.

28. N.A.S. Webster, C.D. Ling, C.L. Raston, F.J. Lincoln, *Solid State Ionics*, 178 (2007) 1451

29. N.A.S. Webster, C.D. Ling, C.L. Raston, F.J. Lincoln, *Solid State Ionics*, 179 (2008) 697

30. N.A.S. Webster, K.J. Hartlieb, P.J. Saines, C.D. Ling, F.J. Lincoln, *Mater. Res. Bull*., 46 (2011) 538.

31. J.R. Dygas, P. Kurek, M.W. Breiter, *Electrochim. Acta*, 40 (1995) 1545.

32. M. Malys, J.R. Dygas, M. Holdynski, A. Borowska-Centkowska, W. Wrobel, M. Marzantowicz, *Solid State Ionics*, 225 (2012) 493.

33. A. C. Larson, R. B. Von Dreele, Los Alamos National Laboratory Report, No. LAUR-86-748, (1987).

34. D.A. Shirley, *Phys. Rev. B*, 5 (1972) 4709.

35. R.D. Shannon, *Acta Crystallogr*. A32 (1976) 751.

36. M. Holdynski, M. Sintyureva, X. Liu, W. Wrobel, J.R. Dygas, M.Pisarek, R.M. Nix, F. Krok, I Abrahams, *J. Phys.: Condens. Matter* 24 (2012) 045904.

37. K.S. Kim, T.J. O'Leary, N. Winograd, *Analyt. Chem*., 45 (1973) 2214.

38. W.E. Morgan, W.J. Stec, J.R. van Wazer, *Inorg. Chem.* 12 (1973) 953.

39. G.P. Kostikova, D.V. Korolkov, Yu.P. Kostikov, *Russ. J. Gen. Chem*., 71 (2001) 1010.

40. A.A. Zav'yalova, R.M. Imamov, Z.G. Pinsker, *Kristallografiya*, 10 (1965) 480.

41. I.N. Tang, A.W. Castleman, *J. Chem. Phys*. 60 (1974) 3981.

42. A. Ferrari, Gazz. Chim. Italiana, 56 (1926) 630.

43. H.C. Roberts, R.S. Eachus, J. Chem. Phys., 57 (1972) 3022.

44. I.N. Tang, A.W. Castleman, *J. Chem. Phys*. 57 (1972) 3638.

45. I. Abrahams, A. Kozanecka-Szmigiel, F. Krok, W. Wrobel, S.C.M. Chan, J.R. Dygas, *Solid State Ionics* 177 (2006) 1761.

46. J. C. Fuggle, N. Martensson, *J. Electron Spectrosc. Relat. Phenom.*, **21** (1980) 275.

47. V.S. Dharmadhikari, S.R. Sainkar, S. Badrinarayan, A. Goswami, *J. Electron Spectrosc. Relat. Phenom.* 25 (1982) 181.

48. V.I. Nefedov, D. Gati, B.F. Dzhurinskii, N.P. Sergushin, Y.V. Salyn, *Zh. Neorg. Khim.* 20 (1975) 2307.

49. T.P. Debies, J.W. Rabalais, *Chem. Phys.* 20 (1977) 277.

50. Y. Schuhl, H. Baussart, R. Delobel, M. Le Bras, J. Leroy, L.G. Gengembre, J. Rimblot, *J. Chem. Soc. Faraday Trans*., *I* 79 (1983) 2055.

51. S. Rondon, P.M.A. Sherwood, *Surf. Sci. Spectra*, 5 (1998) 97.

52. H. Kanai, M. Yoshiki, M. Hayashi, R. Kuwae, Y. Yamashita, *J. Am. Ceram. Soc*., 77 (1994) 2229.

53. G. Gokagac, B.J. Kennedy, *J. Electroanal. Chem.* 353 (1993) 71.

54. C. Hinnen, C.N. van Huong, P. Marcus, *J. Electron Spectrosc. Relat. Phenom*., 73 (1995) 293.

55. S. Rondon, P.M.A. Sherwood, *Surf. Sci. Spectra*, 5 (1998) 104.

56. R.P. Vasquez, M.C. Foote, B.D. Hunt, *J. Appl. Phys*., 66 (1989) 4867.

57. A.E. Hughes, B.A. Sexton, *J. Electron Spectrosc. Relat. Phemon.*, 50 (1990) c15.

58. Y. Uwamino, Y. Ishizuka, H. Yamatera, *J. Electron Spectrosc. Relat. Phenom*., 34 (1984) 69.

59. A. Gauzzi, H.J. Mathieu, J.H. James, B. Kellett, *Vacuum*, 41 (1990) 870.

Table 1

Temperatures for endothermic event maxima from DTA analysis of $Bi_{2.5+x}Pb_{0.5}YO_{5.75+3x/2-\delta}$

x	T_1 [°C]	T_2 [°C]
0	401	595
1	394	573
2	393	562

Table 2

XPS binding energies (eV) for $Bi_{2.5+x}Pb_{0.5}YO_{5.75+3x/2-\delta}$. Estimated standard deviations are given in parentheses. Selected literature values are included for comparison.

Formula	Bi $4f_{7/2}$	Bi $4f_{5/2}$	Pb $4f_{7/2}$	Pb $4f_{5/2}$	Y $3d_{5/2}$	Reference
$Bi_{2.5}Pb_{0.5}YO_{5.75}$	158.68(1)	164.04(1)	137.89(1)	142.78(1)	157.1(2)	This work
$Bi_{3.5}Pb_{0.5}YO_{7.25}$	158.83(1)	164.17(1)	137.97(1)	142.87(1)	157.4(2)	This work
$Bi_{4.5}Pb_{0.5}YO_{8.75}$	158.94(1)	164.27(1)	138.12(1)	143.02(1)	157.4(2)	This work
Bi	157.0	162.3				[46]
Bi_2O_3	158.6-159.8	163.6-165.1				[38,47-50]
$NaBiO_3$	159.3	164.5				[38]
$NaBiO_3$	157.6					[39]
Pb			136.9	141.7		[46]
PbO			137.7-138.2	142.9		[39, 51-54]
PbO_2			137.3	142.1		[55]
Y_2O_3					156.6-157.0	[56-59]

Table 3

Electrical parameters (σ_{300} = conductivity at 300°C; σ_{800} = conductivity at 800°C; ΔE_{LT} = low temperature activation energy; ΔE_{HT} = high temperature activation energy) for compositions in the $Bi_{2.5+x}Pb_{0.5}YO_{5.75+3x/2-\delta}$ system. Estimated standard deviations are given in parentheses.

x	ΔE_{LT} /eV	σ_{300} /S cm^{-1}	ΔE_{HT} /eV	σ_{800} /S cm^{-1}
0	1.376(1)	$5.3(2) \times 10^{-6}$	0.768(1)	0.353(5)
1	1.189(2)	$2.0(6) \times 10^{-5}$	0.638(1)	0.423(4)
2	1.380(1)	$1.3(3) \times 10^{-5}$	0.605(1)	0.295(4)

Figure captions

Fig. 1. X-ray powder diffraction patterns for $Bi_{2.5+x}Pb_{0.5}YO_{5.75+3x/2-\delta}$ at room temperature and 700°C.

Fig.2. Variation of cubic lattice parameter, *a*, at selected temperatures as a function of average cation radius (values based on weighted average of ionic radii for six coordination [35]).

Fig. 3. Thermal variation of cubic lattice parameter, *a*, from Rietveld analysis of X-ray powder diffraction for $Bi_{2.5+x}Pb_{0.5}YO_{5.75+3x/2-\delta}$ on heating (filled symbols) and cooling (open symbols).

Fig. 4. DTA thermograms for $Bi_{2.5+x}Pb_{0.5}YO_{5.75+3x/2-\delta,}$ with detail of the heating profiles inset.

Fig. 5. Thermogravimetric curves for $Bi_{2.5+x}Pb_{0.5}YO_{5.75+3x/2-\delta}$. Dashed and solid lines show heating and cooling runs, respectively.

Fig. 6. Fitted XPS spectra for $Bi_{2.5+x}Pb_{0.5}YO_{5.75+3x/2-\delta}$, showing (a) Bi $4f_{7/2}$ and $4f_{5/2}$ with Y $3d_{3/2}$ and $3d_{5/2}$, (b) Pb $4f_{7/2}$ and $4f_{5/2}$ and (c) O 1*s* emissions.

Fig. 7. Arrhenius plots of total conductivity for $Bi_{2.5+x}Pb_{0.5}YO_{5.75+3x/2-\delta}$. Data corresponding to the second cooling cycle are shown.

Fig. 8. Contributions of electronic and ionic conductivity to total conductivity in (a) $x = 0$ and (b) $x = 2$ compositions of $Bi_{2.5+x}Pb_{0.5}YO_{5.75+3x/2-\delta}$.

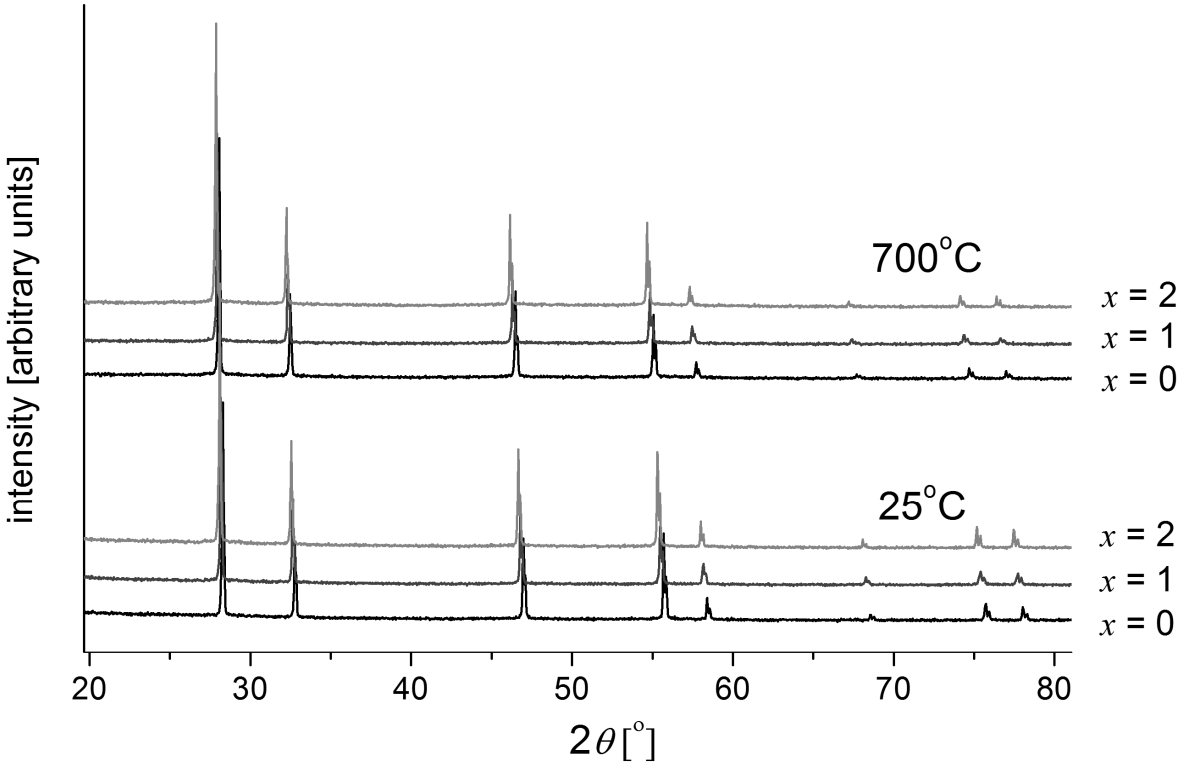

Fig. 1. X-ray powder diffraction patterns for $Bi_{2.5+x}Pb_{0.5}YO_{5.75+3x/2-\delta}$ at room temperature and 700°C.

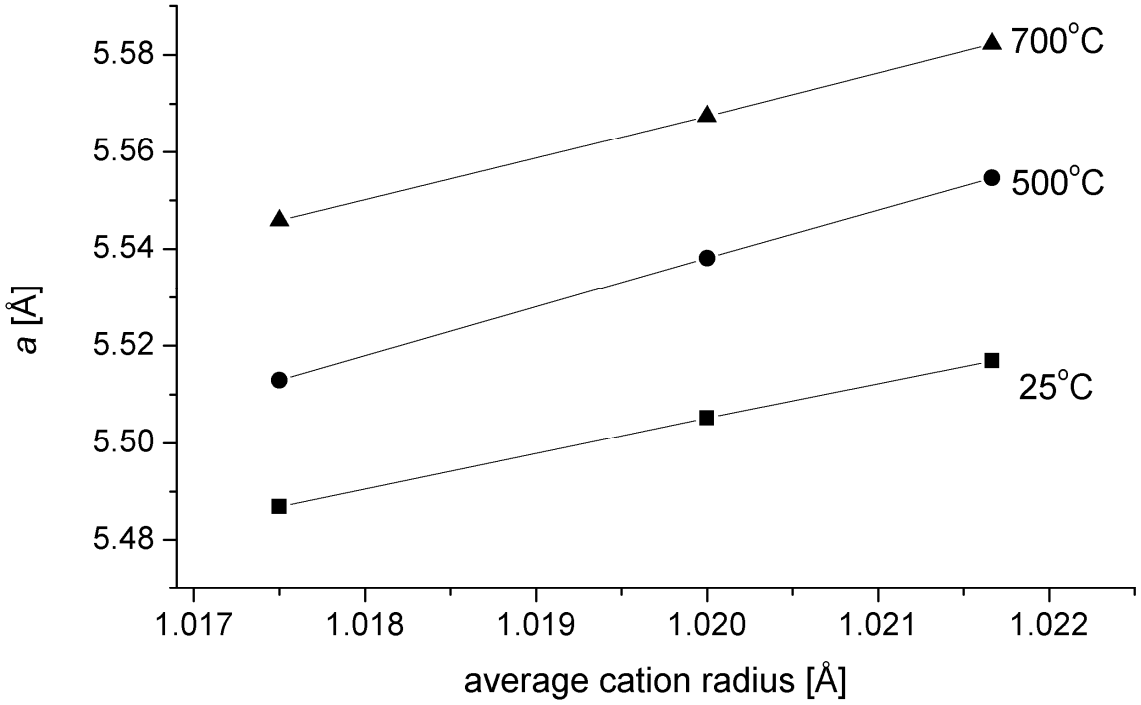

Fig.2. Variation of cubic lattice parameter, *a*, at selected temperatures as a function of average cation radius (values based on weighted average of ionic radii for six coordination [35]).

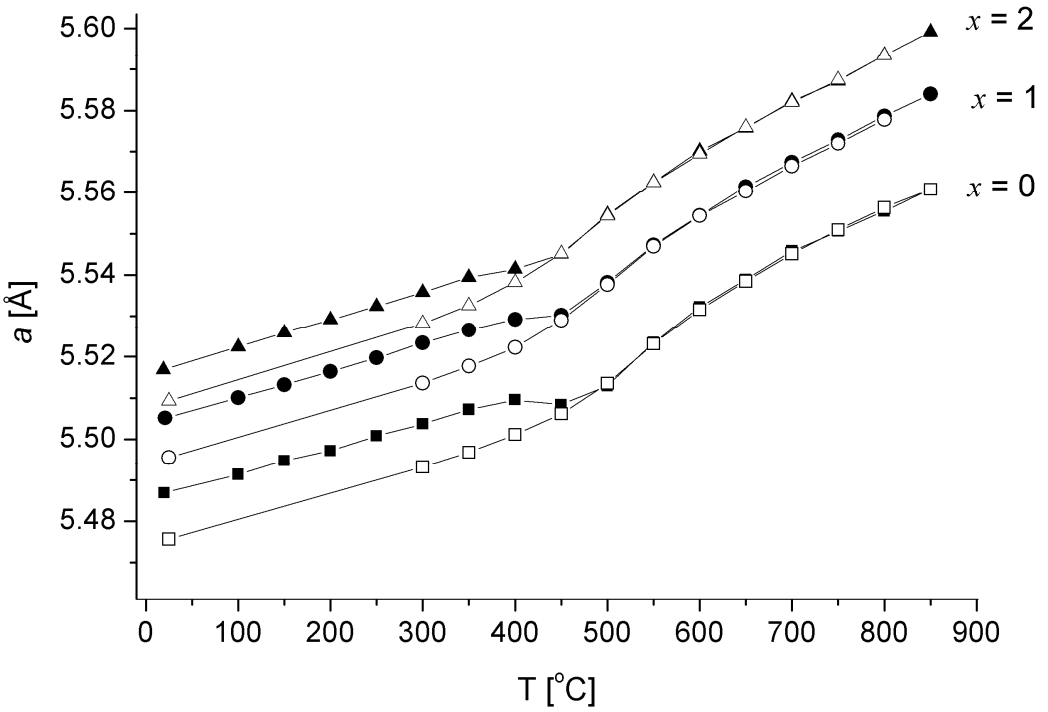

Fig. 3. Thermal variation of cubic lattice parameter, *a*, from Rietveld analysis of X-ray powder diffraction for $Bi_{2.5+x}Pb_{0.5}YO_{5.75+3x/2-\delta}$ on heating (filled symbols) and cooling (open symbols).

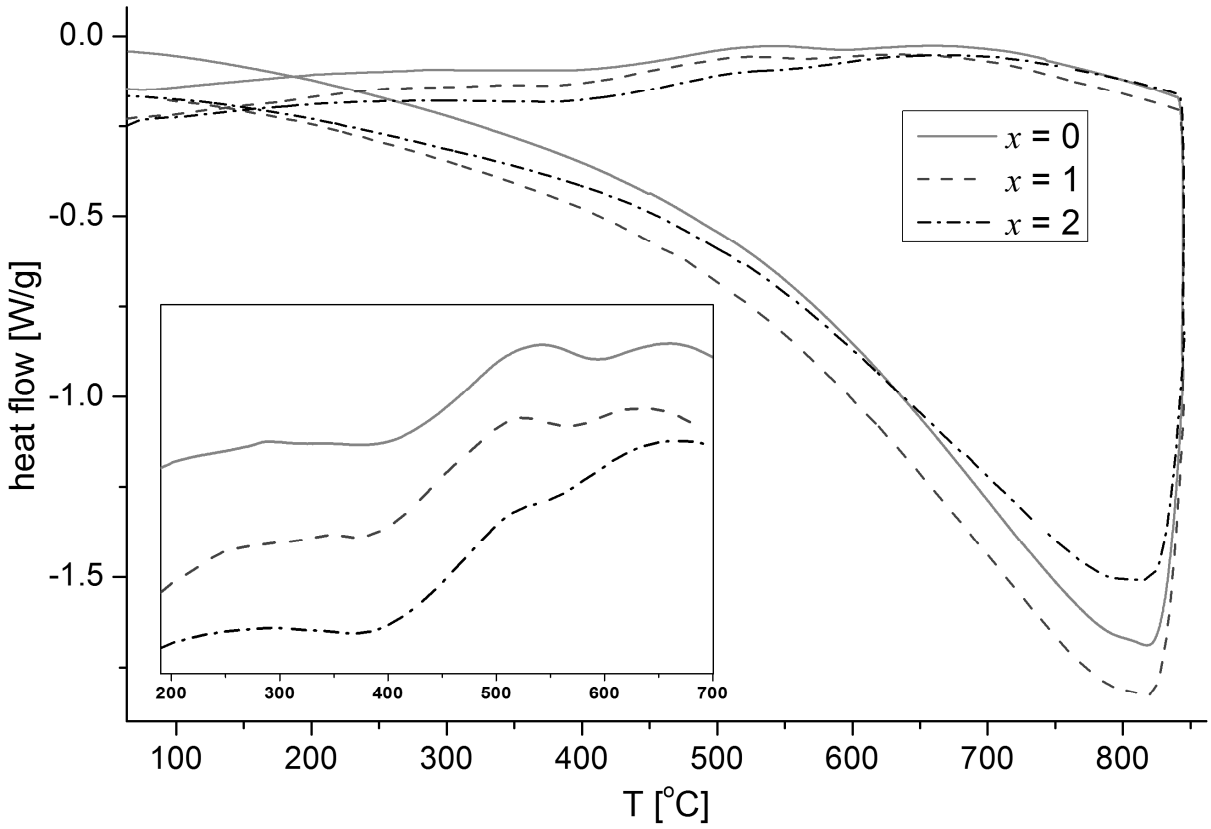

Fig. 4. DTA thermograms for $Bi_{2.5+x}Pb_{0.5}YO_{5.75+3x/2-\delta,}$ with detail of the heating profiles inset.

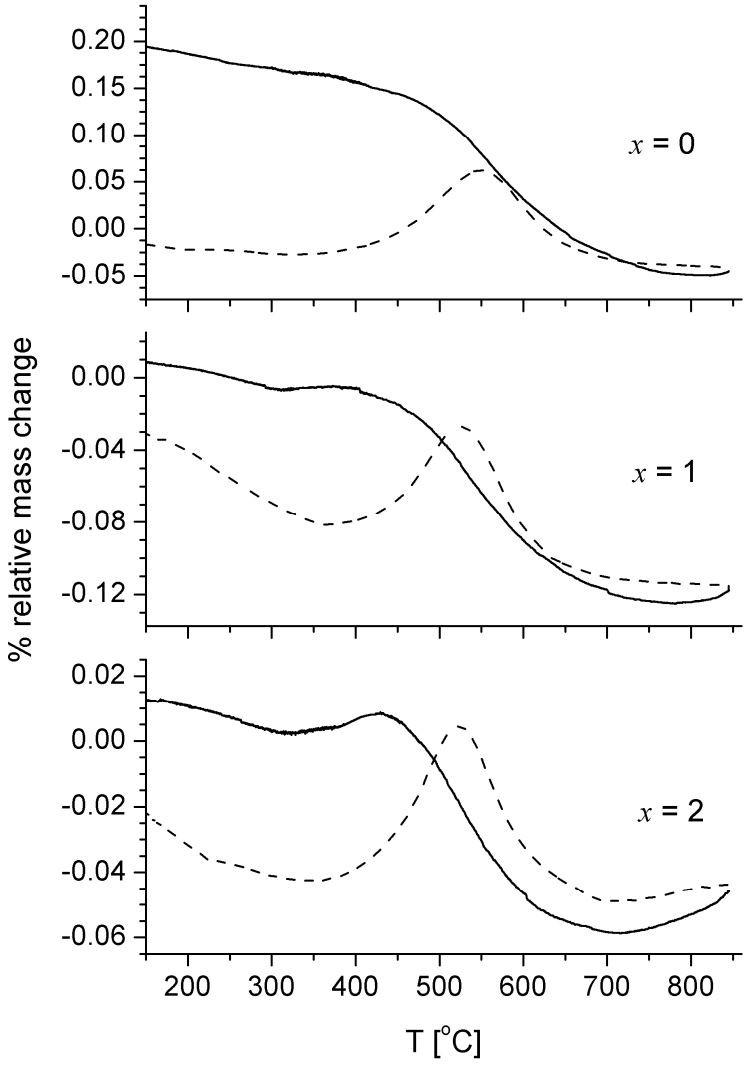

Fig. 5. Thermogravimetric curves for $Bi_{2.5+x}Pb_{0.5}YO_{5.75+3x/2-\delta}$. Dashed and solid lines show heating and cooling runs, respectively.

(a)

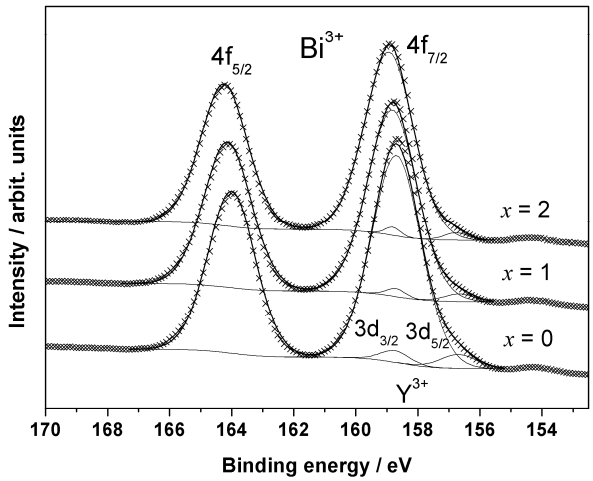

(b)

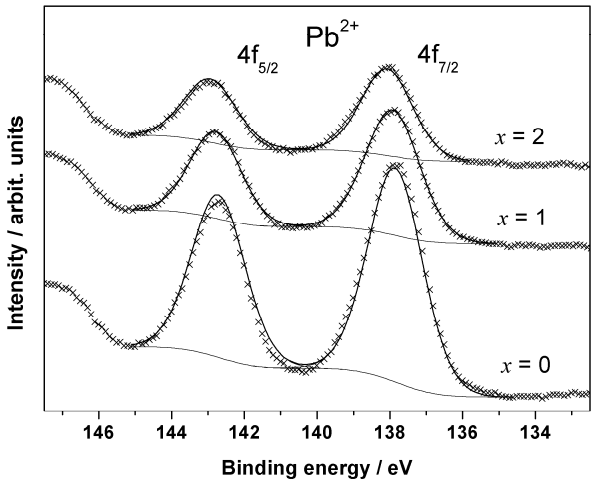

(c)

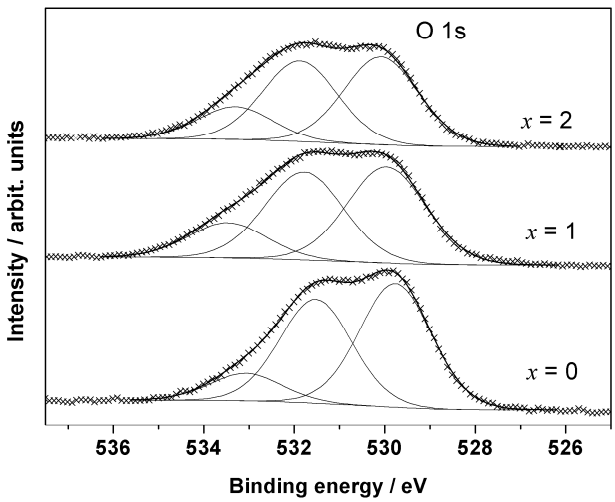

Fig. 6. Fitted XPS spectra for $Bi_{2.5+x}Pb_{0.5}YO_{5.75+3x/2-\delta}$, showing (a) Bi $4f_{7/2}$ and $4f_{5/2}$ with Y $3d_{3/2}$ and $3d_{5/2}$, (b) Pb $4f_{7/2}$ and $4f_{5/2}$ and (c) O 1*s* emissions.

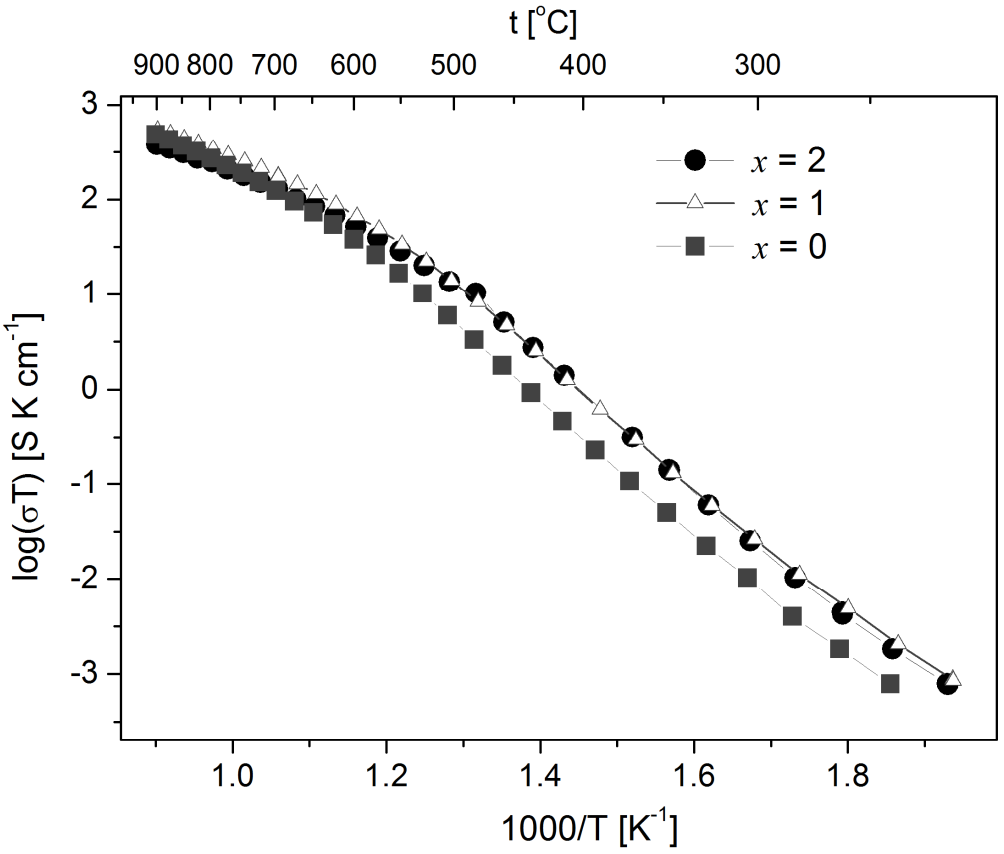

Fig. 7. Arrhenius plots of total conductivity for $Bi_{2.5+x}Pb_{0.5}YO_{5.75+3x/2-\delta}$. Data corresponding to the second cooling cycle are shown.

(a)

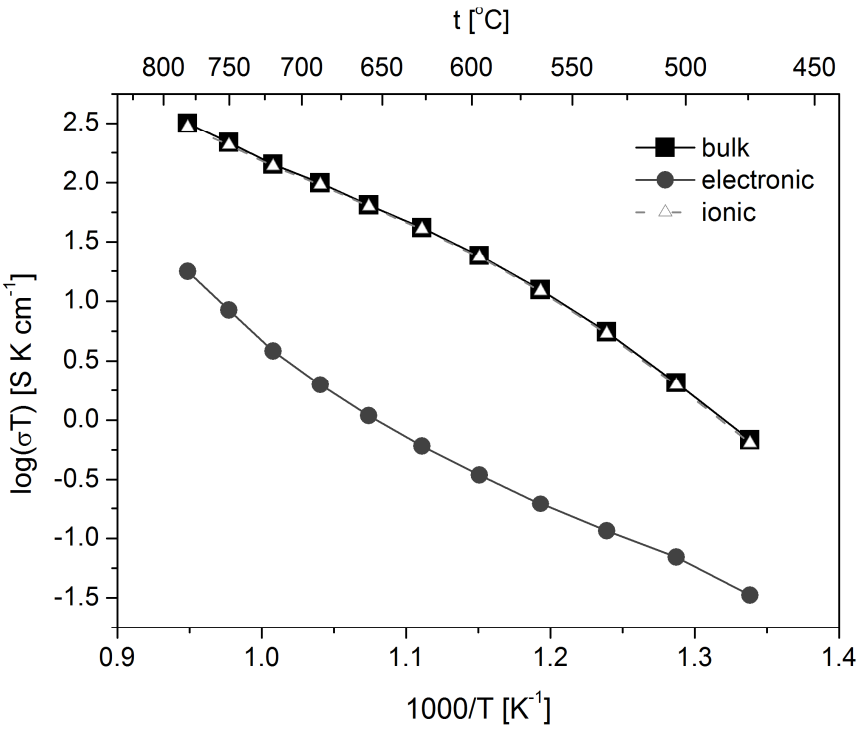

(b)

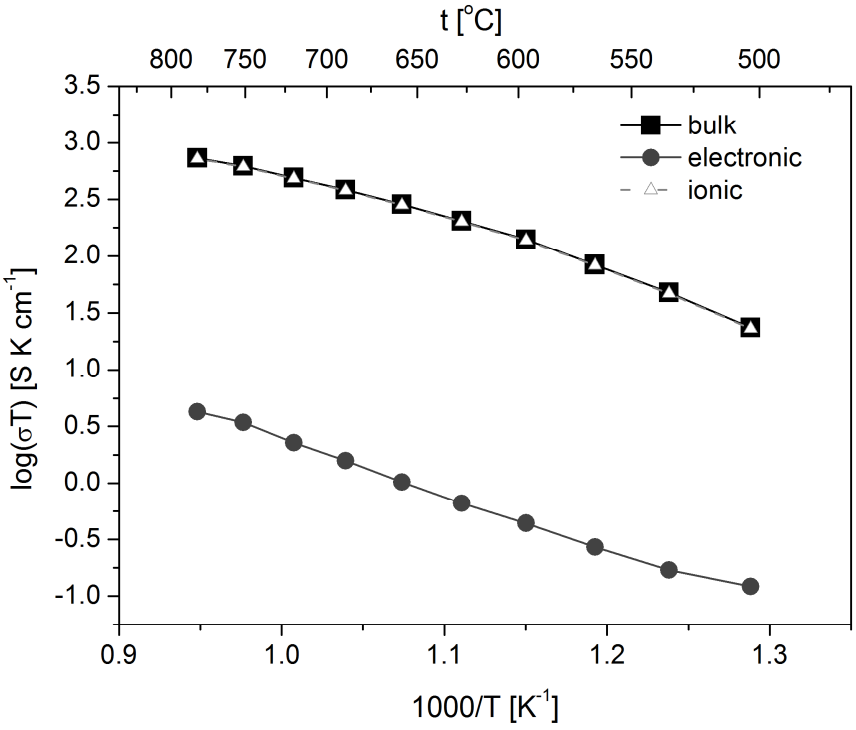

Fig. 8. Contributions of electronic and ionic conductivity to total conductivity in (a) $x = 0$ and (b) $x = 2$ compositions of $Bi_{2.5+x}Pb_{0.5}YO_{5.75+3x/2-\delta}$.